Article ID: 1006-8775(2020) 03-0300-11

An Algorithm for Detecting Ice Cloud at Different Altitudes by Combining Dual CrIS Full Spectrum Resolution CO_2 Channels

WANG Li-wen (王立稳)[1, 2], ZHENG You-fei (郑有飞)[2], TIAN Miao (田 淼)[3], XU Jing-xin (徐静馨)[4]
(1. Key Laboratory for Aerosol-Cloud-Precipitation of China Meteorological Administration, Nanjing University of Information Science & Technology, Nanjing 210044 China; 2. Jiangsu Collaborative Innovation Center of Atmospheric Environment and Equipment Technology, Nanjing University of Information Science & Technology, Nanjing 210044 China; 3. Information Engineering Department, School of Information and Communication Engineering, University of Electronic Science and Technology of China, Chengdu 611731 China; 4. State Environmental Protection Key Laboratory of Atmospheric Physical Modeling and Pollution Control, State Power Environmental Protection Research Institute, Nanjing 210031 China)

Abstract: Using infrared sensors to detect ice clouds in different atmospheric layers is still a challenge. The different scattering and absorption properties of longwave and shortwave infrared channels can be utilized to fulfill this purpose. In this study, the release of Suomi-NPP Cross-track Infrared Sounder (CrIS) full spectrum resolution is used to select and pair channels from longwave (~ 15 μm) and shortwave (~4.3 μm) CO_2 absorption bands under stricter conditions, so as to better detect ice clouds. Besides, the differences of the weighting function peaks and cloud insensitive level altitudes of the paired channels are both within 50 hPa so that the variances due to atmospheric conditions can be minimized. The training data of clear sky are determined by Visible Infrared Imaging Radiometer Suite (VIIRS) cloud mask product and used to find the linear relationship between the paired longwave and shortwave CO_2 absorption channels. From the linear relationship, the so-called cloud emission and scattering index (CESI) is derived to detect ice clouds. CESI clearly captures the center and the ice cloud features of the Super Typhoon Hato located above 415 hPa. Moreover, the CESI distributions agree with cloud top pressure from the VIIRS in both daytime and nighttime in different atmospheric layers.

Key words: Cross-track Infrared Sounder Full Spectral Resolution (CrIS FSR); ice cloud detection; dual CO_2 absorption bands

CLC number: P412.27 **Document code:** A

https: //doi.org/10.46267/j.1006-8775.2020.027

1 INTRODUCTION

Ice clouds cover almost 20% of the globle (Sassen et al. [1]). They can regulate the Earth's radiation budget by absorbing thermal infrared radiation emitted from the lower atmosphere and the Earth's surface and reflecting solar radiation (Liou [2]; Stephens et al. [3]).

Infrared (IR) channels have been widely used to detect clouds. Most studies used window channels located from 8 to 12 μm to detect clouds, especially ice clouds, by using their brightness temperature difference (Inoue [4]; Ackerman et al. [5]; Parol et al. [6]; Giraud et al. [7]; Chiriaco et al. [8]), which has been applied to many imager sensors to detect clouds (e. g. Moderate-resolution Imaging Spectroradiometer, MODIS) (Prabhakar et al. [9]; Heidinger et al. [10]; Wang et al. [11]; Kopp et al. [12]). Moreover, Ou et al. used two mid-IR atmospheric window (5.1-5.3 and 3.7 μm) bands to derive ice cloud properties [13]. In addition to cloud detection by using imagers, a method based on the departure between observed and simulated radiance was developed by McNally and Watts to help hyperspectral infrared sounders detect clouds [14].

Even though ice clouds and their properties can be derived from the brightness temperature of infrared window channels, it is still challenging to detect clouds from the IR channels in certain vertical atmospheric layers. However, the strong absorption channels of carbon dioxide (CO_2) in IR channels provide an opportunity to detect radiation from a high level in the atmosphere. This is because CO_2 is almost uniformly mixed in the atmosphere and atmospheric temperature profiles over the globe are provided by them (Menzel et al. [15]). There are two main CO_2 IR absorption bands. In the CO_2 slicing method, the CO_2 IR absorption bands located near 15 μm are used to derive cloud altitude and atmospheric temperature profiles (Chahine [16]; Smith and Platt [17]; Menzel et al. [18]; Smith and Frey [19]). The shortwave CO_2 (~4.3 μm) absorption bands are used to obtain upper atmospheric temperature. Gao et al. combined CO_2 (~4.3 μm) bands with N_2O, and its

Received 2019-11-12 **Revised** 2020-05-15 **Accepted** 2020-08-15

Funding: National Key R&D Program (2018YFC1506904); Natural Science Foundation of China (41590873, 41705089)

Biography: WANG Li-wen, Ph. D., primarily undertaking research on satellite remote sensing.

Corresponding author: ZHENG You-fei, e-mail: zhengyf@nuist.edu.cn

properties were similar to that of the 15 μm CO_2 channels [20].

In 2017, Lin et al. (hereinafter referred to as L17) developed a new algorithm by using the Cross-track Infrared Sounder (CrIS) longwave (~15 μm) and shortwave (~4.3 μm) CO_2 absorption bands to detect clouds in different atmospheric levels [21]. It is based on the differences in the scattering and emission characteristics of the longwave and shortwave CO_2 channels at certain atmospheric altitude. In L17, due to the lack of local time information in the simulation, the algorithm neglected the shortwave infrared (wavenumber 2200~2400 cm^{-1}, SWIR) data that were affected by solar radiation in the daytime. Moreover, the calculation of insensitive cloud altitude was not as strict as longwave, which made the brightness temperature of SWIR more sensitive to clouds than that of longwave infrared (wavenumber 670~760 cm^{-1}, LWIR) channels. Besides, by the time of L17, the CrIS full spectrum resolution (FSR) data was not available.

In order to use the observed brightness temperature to derive cloud detection, the observational clear sky data are used to pair the relationship between the LWIR and SWIR channels, compared with the simulation in L17. Also, this study adds more paired channels for high cloud detection due to the use of FSR channels. The conditions of cloud insensitive level for SWIR is stricter than those of L17.

The paper is organized as follows: Section 2 briefly describes the CrIS, VIIRS cloud mask product and the community radiative transfer model (CRTM). Section 3 presents the method of deriving the FSR CESI. Section 4 is the performance assessment of CESI for ice cloud detection. A general conclusion is given in section 5.

2 INSTRUMENT DESCRIPTION AND RADIATIVE TRANSFER MODEL

2.1 *CrIS instrument*

The Cross-track Infrared Sounder (CrIS), on board the Suomi National Polar-Orbiting Partnership (S-NPP) satellite, is a Fourier transform spectrometer. It was launched on October 28, 2011 into an orbit at a nominal altitude of 824 km. S-NPP crosses the equator at 13:30 local time during its ascending node. On November 18, 2017, the NOAA-20 satellite carrying CrIS module 2 was launched. The NOAA-20 has a similar orbit to that of S-NPP except for the ½ orbit along-track separation. The field of view (FOV) of CrIS, arranged into a 3×3 grid, is defined by the sizes and positions of the 9 detector fields. The fields of regards (FOR) is defined by the combined 3×3 FOVs. CrIS collects 30 FORs in the cross-track direction and each FOR contains 3×3 FOVs within the nadir resolution about 14 km (Han et al. [22]). In the normal spectral resolution (NSR), CrIS provides 1, 305 channels for atmospheric sounding in three spectral bands: the long-wave IR (LWIR) band from 650 to 1, 095 cm^{-1}, middle-wave IR (MWIR) band from 1, 210 to 1,750 cm^{-1}, and short-wave IR (SWIR) band from 2,155 to 2,550 cm^{-1}. The NSR resolution is 0.625, 1.25, and 2.5 cm^{-1} for LWIR, MWIR, and SWIR, respectively. Additionally, CrIS can be operated in the full spectral resolution (FSR) mode as well, at which the spectral resolution for all three bands is 0.625 cm^{-1} and the total number of channels is 2, 211 (Han et al. [22]; Chen et al. [23]; Chen et al. [24]; Han and Chen [25]). The FSR data become available on March 8, 2017, at the NOAA Comprehensive Large Array-data Stewardship System (CLASS).

2.2 *VIIRS cloud mask*

The Visible Infrared Imaging Radiometer Suite (VIIRS) is one of the key instruments onboard the SNPP satellite and the first Joint Polar Satellite System (JPSS-1). It has 22 bands, covering 16 moderate resolution bands ("M" bands) with a spatial resolution from 750 m at the nadir to 1.5 km at the edge, 5 imaging resolution bands ("I" bands) with spatial resolution 375–750 m, and a day-night band, covering from 0.5 to 0.9 μm (Cao et al. [26]). There are four categories of cloud detection indicators for the S-NPP VIIRS Cloud Mask (VCM) product, including confidently cloudy, probably cloudy, probably clear and confidently clear (Hutchison et al. [27]). The agreement of VIIRS CM product with CALIOP is more than 90% in the range of 60°S and 60°N in both day and night (Kopp et al. [12]). Furthermore, the cloud mask quality has four flags: "Poor", "Low", "Medium" and "High". In this paper, VIIRS cloud mask product and VIIRS M15 (~10.763 μm) are employed to collocate with CrIS to obtain the clear field of view (FOV).

2.3 *Community radiative transfer model*

A fast radiative transfer model named Community Radiative Transfer Model (CRTM) is used to simulate the infrared and microwave satellite radiances (Weng et al. [28]). The input profiles to CRTM are atmospheric profiles including pressure, temperature, water vapor, and ozone for each layer and surface variables containing surface temperature. In the calculation of CRTM, the radiative transfer problem is split into several parts, such as gaseous absorption, and cloud absorption/scattering. As for IR sensors, there are three surface emissivity or reflectivity models for inferred land and two models for infrared water. The cloud types in CRTM are water, ice, rain, snow, graupel, and hail (Chen et al. [29]) and the various effective radius is assumed to have Gamma size distribution (Yang et al. [30]). Chen et al. developed both the nonlocal thermodynamic equilibrium (NLTE) and a bidirectional reflectance distribution function (BRDF) to compute the solar refection at shortwave [29]. NLTE and BRDF are implemented into the current version of CRTM. In CRTM, surface emissivity or reflectance are used according to the different surface types for visible, infrared (IR) and microwave sensors, respectively. For IR, the IR Sea Surface Emission Model (IRSSE) model

(van Delst and Wu [31]) is employed. IRSSE model is a parameterized Wu-Smith model (Wu and Smith [32]) for wind-roughened sea surface. In addition, the sensors onboard S-NPP are validated and verified by CRTM (Liu and Boukabara [33]). The latest version v2.3.0, released on April 21st, 2017, adds new coefficients of CrIS full spectrum resolution to calculate the weighting function (WF) and cloud insensitive altitude in this study.

3 METHODS

3.1 *The training data sets*

In L17, the brightness temperature in the clear sky condition is obtained by using CRTM simulation. However, only the 399 CrIS channels used in Gridpoint Statistical Interpolation (GSI) system are covered in L17, resulting in a sparse resolution of shortwave band. Also, due to the lack of local time in the simulation of L17 for the clear sky, the algorithm has neglected the SWIR data affected by solar radiation in the daytime. In this study, the CrIS FSR data are used and eight days spread are randomly chosen in four seasons (04/03/2017, 04/10/2017, 07/13/2017, 07/20/2017, 10/20/2017, 10/22/2017, 01/14/2018, and 01/19/2018). The following requirements are applied: (1) The "confident" clear and high-quality data are selected in VIIRS EDR cloud mask products by collocating CrIS with VIIRS EDR cloud mask products to ensure each selected CrIS FOV is not contaminated by clouds. The collocation between CrIS and VIIRS is fulfilled according to Wang et al. [34], which matches the VIIRS pixels with CrIS FOVs based on the geolocation during the same time. (2) The VIIRS M15 band (~10.763 μm) is employed to reconstruct and compare the collocated *BT* in each CrIS FOV. The standard deviation of M15 *BT* in each collocated CrIS FOV is less than 0.3 K. Based on equation 1, we can derive the reconstructed *BT* and the difference between reconstructed *BT* and M15 *BT* is less than 1K.

$$BT_{\text{reconstruct}} = \frac{\int_{\lambda_1}^{\lambda_2} B(\lambda, T)\,\phi(\lambda)\,\mathrm{d}\lambda}{\int_{\lambda_1}^{\lambda_2} \phi(\lambda)\,\mathrm{d}\lambda}, \tag{1}$$

where $B(\lambda, T)$ is the Planck Function, λ is the wavelength, and ϕ is the response function of VIIRS M15 band.

However, it should be noted that the shortwave channels around 4.0 μm are sensitive to solar radiation in the daytime (McNally and Watts [14]). Therefore, daytime and nighttime are separated in the training data sets and there are a total number of 145, 990 and 190, 074 clear sky FOVs in the daytime and nighttime between 60°S and 60°N, respectively.

3.2 *Pairing LWIR with SWIR*

The steps to find the appropriate pairs between LWIR and SWIR channels are based on L17. First, for both LWIR and SWIR, only the channels with the altitudes of WF peak between 150 hPa and 440 hPa are considered. According to the ISCCP category, high-level clouds whose cloud top pressure above 440 hPa belong to ice clouds (Rossow and Schiffer [35]). The BT is more sensitive to the clouds when clouds located above the WF peak altitude (Weng and Zou [36]). Fig. 1 presents the WFs calculated from an American standard profile for the dual CO_2 bands within their WF peaks within 150 hPa to 440 hPa.

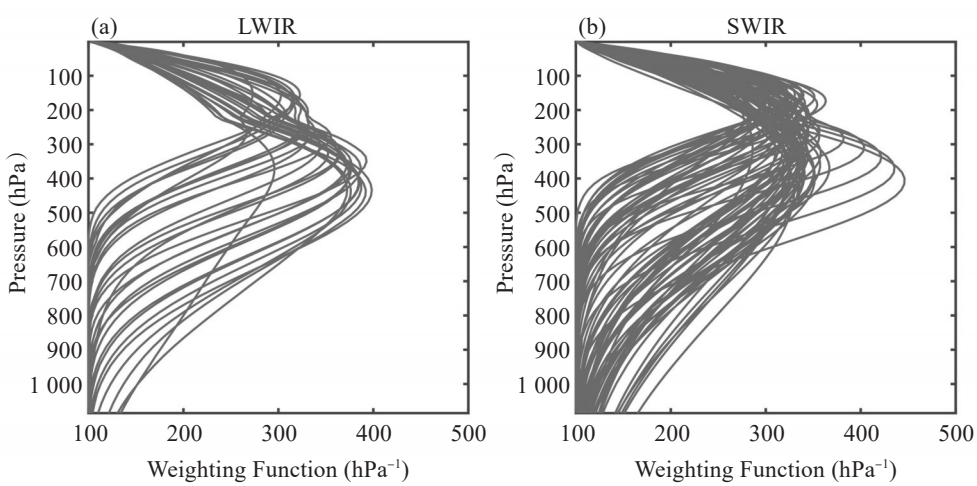

Figure 1. (a) WFs of 30 LWIR and (b) 81 SWIR channels of which the peak WFs are in the range of 150hPa and 440hPa.

Second, the shape of WF is considered in our work as well. This is because the WFs of some channels are broad while some are narrow. For the channels with broad WF shape, radiance is mainly emitted from the deeper atmosphere. On the contrary, radiance comes from the shallower atmospheric layer for the channels with narrow WF (Carrier et al. [37]). To make sure the channels' *BT* are not contaminated by clouds through the low altitude or high pressure tails of their WFs, the cloud-insensitive level defined by McNally and Watt[14] is used as another selecting condition, shown as follows:

$$\frac{\left|R_{\text{clear}} - R_{\text{cloudy}}\right|}{R_{\text{clear}}} \leqslant 0.01, \tag{2}$$

where R_{clear} and R_{cloudy} are the clear-sky radiance and the overcast radiance, respectively. Furthermore, the altitude of WF peak should be higher than the cloud-insensitive height (Chen et al. [24]). The altitude of the peak WF and the cloud-insensitive between LWIR and SWIR channels should be equal to or less than 50 hPa away from each other. These requirements can minimize the variances of the atmospheric conditions. The numbers of LWIR and SWIR channels meeting the requirements are 16 and 10, respectively. Fig. 2 shows the variation of the ratio $\frac{|R_{clear} - R_{cloudy}|}{R_{clear}}$ for 16 LWIR and 10 SWIR channels. The cloud insensitive levels of 16 LWIR and 10 SWIR channels are mainly in the range of 330 and 1,000 hPa when radio of radiance is 0.01.

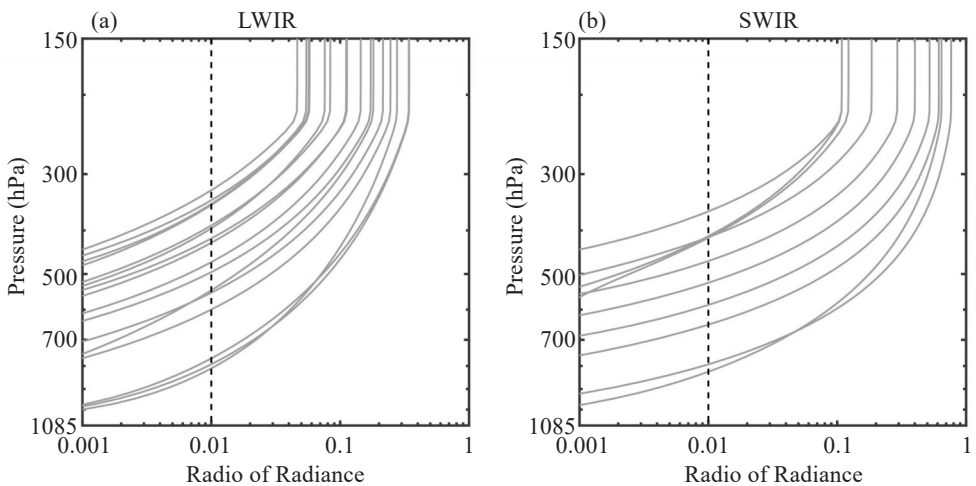

Figure 2. Ratio of radiance for 16 LWIR (a) and 10 SWIR (b) with their cloud-insensitive level less than peak WF altitude.

Finally, the number of LWIR and their corresponding candidate SWIR channels are not only one and vice versa. The training data are used to calculate the correlation coefficients of the candidate LWIR and SWIR channel pairs. Fig. 3 shows the correlation coefficients of these candidate LWIR and SWIR channel pairs. For pairs that have common channels, the one with maximum correlation coefficients is kept for this study. After the three steps above, the paired LWIR and SWIR are shown in Table 1.

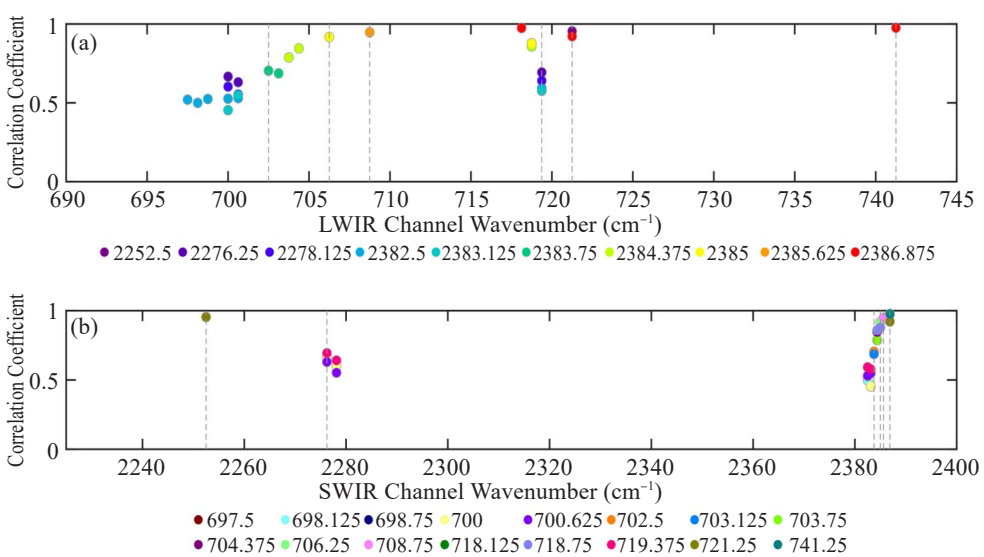

Figure 3. (a) Correlation coefficient between LWIR channels and their corresponding SWIR channels; (b) correlation coefficient between SWIR channels and their corresponding LWIR channels.

3.3 *The Cloud Emission and Scattering Index*

When pairing LWIR and SWIR channels are determined, we assume the brightness temperature of LWIR and SWIR channels are linearly proportional and can be established by a linear regression model.

$$BT^{SWIR}_{i,regression} = \alpha_i BT^{LWIR}_{i,clear} + \beta_i, \quad (3)$$

where the subscript "i" represents the number of pairs. α and β are the regression coefficients, BT^{LWIR}_{clear} and BT^{SWIR}_{clear}

Table 1. The channel number, wavenumber, WF peak altitude and cloud-insensitive height for six paired LWIR and SWIR channels.

Pair	LWIR				SWIR			
	Channel Number	Wave Number	Peak WF Height	Cloud-insensitive Height	Channel Number	Wave Number	Peak WF Height	Cloud-insensitive Height
1	112	719.375	155.881	399.183	1773	2276.25	165.287	415.972
2	85	702.5	279.59	433.175	1945	2383.75	253.689	468.836
3	91	706.25	351.292	565.345	1947	2385	307.068	585.914
4	115	721.25	366.845	814.868	1735	2252.5	321.406	840.076
5	95	708.75	382.808	606.907	1948	2385.625	336.146	650.164
6	147	741.25	433.175	790.077	1950	2386.875	399.183	814.868

are the brightness temperatures for LWIR and SWIR channels under clear sky conditions.

Figure 4 provides the scattplots of CrIS observed *BT* for six paired LWIR and SWIR channels at nadir FORs for the center FOV in the descending orbits.

The conceptual model named Cloud Emission and Scattering Index (CESI) is defined as follows (Lin et al. [21]; Han et al. [38]).

$$CESI = BT_{\text{obs}}^{\text{SWIR}} - BT_{\text{regression}}^{\text{SWIR}}, \quad (4)$$

where $BT_{\text{regression}}^{\text{SWIR}}$ is the regression of the *BT* of SWIR channels in equation 3 and $BT_{\text{obs}}^{\text{SWIR}}$ is the observational SWIR *BT*.

The CESI reflects the linear relationship between LWIR and SWIR CO_2 absorption bands in the clear and cloudy skies, which are based on the different cloud scattering and emission characteristics. When under the clear sky condition, CESI values are around 0 K. However, when ice clouds exist, the *BT*s of SWIR channels are larger than that of LWIR channels due to the difference of the emissivity between SWIR and LWIR channels. According to Wang et al. [39, 40] and Niu and Zou [41], when ice clouds exist, the CESI values are positive. On the contrary, the value of each CESI is negative or around 0 K when water clouds exist. Therefore, the CESI is more sensitive in detecting ice clouds.

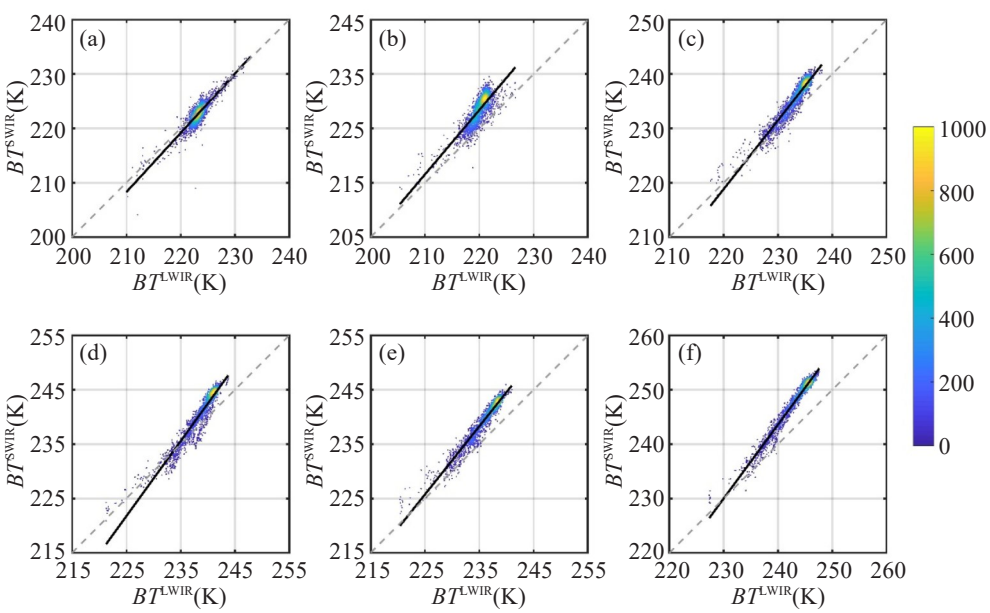

Figure 4. Scatterplots of BT of LWIR and six paired SWIR at nadir FORs for the center FOV in the descending node of orbit in the clear sky. Shading indicates counts of BT.

4 THE PERFORMANCE OF CESI DETECTION

4.1 *The global distribution compared with AIRS*

In order to better show the performance of ice cloud detection in different layers, three pairs of CESI are selected. The selected pairs are Pair-1, Pair-3, and Pair-6, of which the corresponding WF altitudes are around 160 hPa, 320 hPa, 415 hPa, respectively. Fig. 5 shows global distributions of the three selected pairs of CESI and AIRS cloud top pressure at both ascending

nodes (a-d) and descending nodes (e-h). The spatial distributions of CESI in three atmospheric layers agree with the cloud top pressure from AIRS in both of ascending and descending nodes, which indicates that the CESI has the ability to detect ice clouds, especially for the ice clouds located in the tropical regions. Furthermore, the values of CESI gradually increase with the decrease of WF altitude for selected pairs. Additionally, the values of CESI in the ascending nodes are larger than those in the descending nodes due to the solar radiation effect on SWIR channels. However, some ice clouds located in the mid-latitude are missed by CESI.

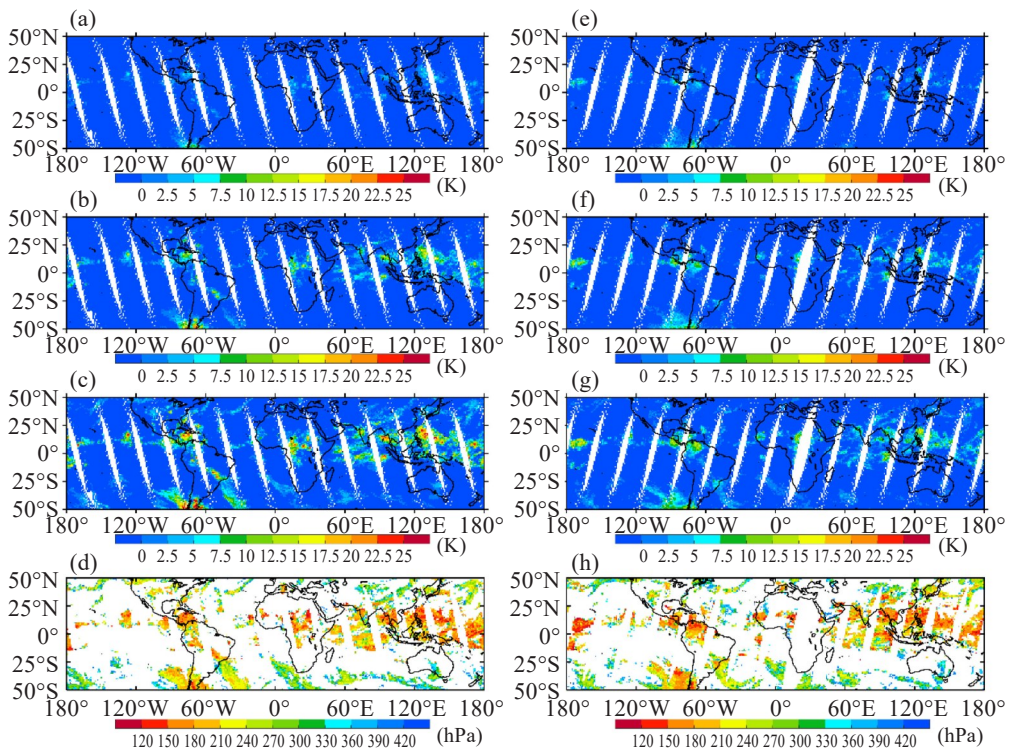

Figure 5. Global distribution of selected three pairs of CESI and AIRS cloud top pressure on 20 August, 2017. (a)-(d) are the ascending nodes while (e)-(h) are the descending nodes. (a) and (e) are Pair-1 (WFP~160 hPa); (b) and (f) are Pair-3 (WFP~320 hPa); (c) and (g) are Pair-6 (WFP~415 hPa); (d) and (h) are the AIRS cloud top pressure (above 420 hPa).

4.2 *The ice cloud detection of Typhoon Hato*

We further apply CESI to Typhoon Hato, as an example, to demonstrate its performance in detecting ice clouds in three selected layers. The cloud top pressure from VIIRS and cloud types and ice optical depth from Advance Himawari Imager (AHI) are employed to be compared with CESIs.

Super Typhoon Hato, a powerful typical cyclone, struck southern China in August 2017. It formed as a tropical depression over the eastern region of Luzon Island on August 19 and quickly developed into a tropical storm. Hato was one of the strongest typhoons that have hit Macau and Hong Kong in the past 50 years, causing a total economic loss of ~ $6.82 billion US dollars along its path. S-NPP CrIS observed the Super Typhoon Hato twice a day ascendingly (UTC 05:50) and descendingly (UTC 17: 40) over the South China Sea region, respectively. Fig. 6 shows the spatial distribution of selected CESIs and cloud top pressure from VIIRS cloud product. Overall, the center and cloud feature of Hato are detected by selected CESI with their WF peak at ~160 hPa (Fig. 6a), ~320 hPa (Fig. 6b), and ~415 hPa (Fig. 6c). The distribution of selected CESIs is relatively consistent with averaged cloud pressure from VIIRS product at three different altitudes. The center of Hato is not shown for VIIRS cloud top pressure. This is because the retrieval of EDR products are not applicable (the values are 65,535 in the EDR products). The CESIs are not distributed uniformly, especially for the center of Hato. One of the reasons is the noise of SWIR (Kahn et al. [42]). However, some clouds located over land and north of Hato are not detected obviously. Fig. 7 is the spatial distribution of the Near Constant Contrast (NCC) EDR product during the nighttime on 20 August 2017. The NCC EDR is employed to display the DNB data easily under all natural light conditions. The "pseudo-albedo" from NCC product shows the center of Hato cloud system is near the Philippines and some parts of clouds locate in the South China Sea and Northwestern Pacific Ocean. The pattern of cloud distribution is satisfactory with Pair-6 around 415hPa in the evening on 20 August 2017 (Fig. 6c).

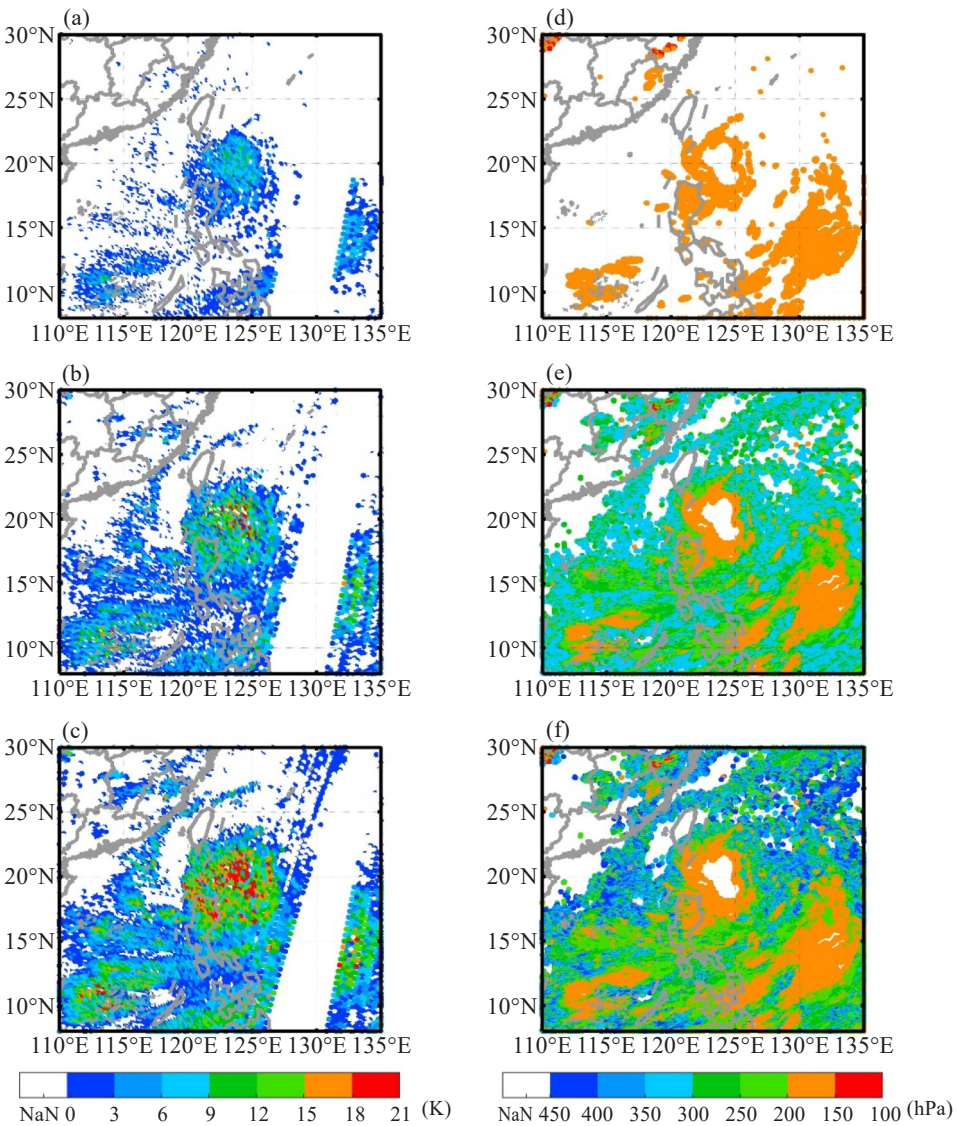

Figure 6. The spatial distribution of three pairs of CESI for the descending nodes and cloud top pressure from VIIRS cloud product at 17:38 on August 20, 2017: (a) Pair-1 with WF peak ~160hPa; (b) Pair-2 with WF peak~320hPa; (c) Pair-6 with peak WF ~ 415hPa; (d) cloud top pressure above 160hPa; (e) cloud top pressure above 320hPa; (f) cloud top pressure above 415hPa.

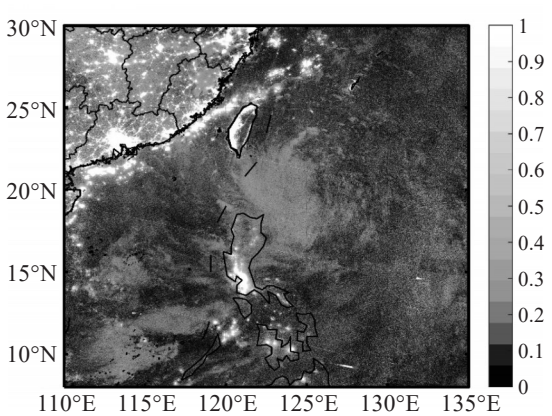

Figure 7. Spatial distribution of VIIRS Near Constant Contrast EDR product on 20 August 2017.

As Hato moved towards the Pearl River estuary on 23 August, its intensity increased and it became a super typhoon. Fig. 8 shows the spatial distribution of Hato by the three selected pairs of CESI and corresponding cloud top pressure from VIIRS EDR product at 05: 46 UTC on 23 August, 2017. It shows that the spatial distributions of CESI in the three layers mostly agree with cloud top pressure from VIIRS. The larger values of CESI, the higher cloud top pressure. The center and cloud features of Typhoon Hato can be revealed by CESI spatial distribution. The selected three pairs of CESI located in different layers also can present a vertical continuity of ice clouds. It shows the CESI with lower WF peak altitude has broader cloud coverage and clouds located oversea are obviously detected by CESIs as well. Fig. 9 shows the cloud type and cloud depth product from Himawari-8. The cloud features around the center of Typhoon Hato are categorized as deep convection with the cloud optical depth above 100. The larger CESI values represent clouds with higher optical thickness (Fig. 9b). Moreover, some cirrostratus and cirrus (Fig.

9a) around the center of Typhoon Hato are also detected by CESIs. Compared with Fig. 9, the values of CESI are associated with cloud optical depth and cloud top pressure.

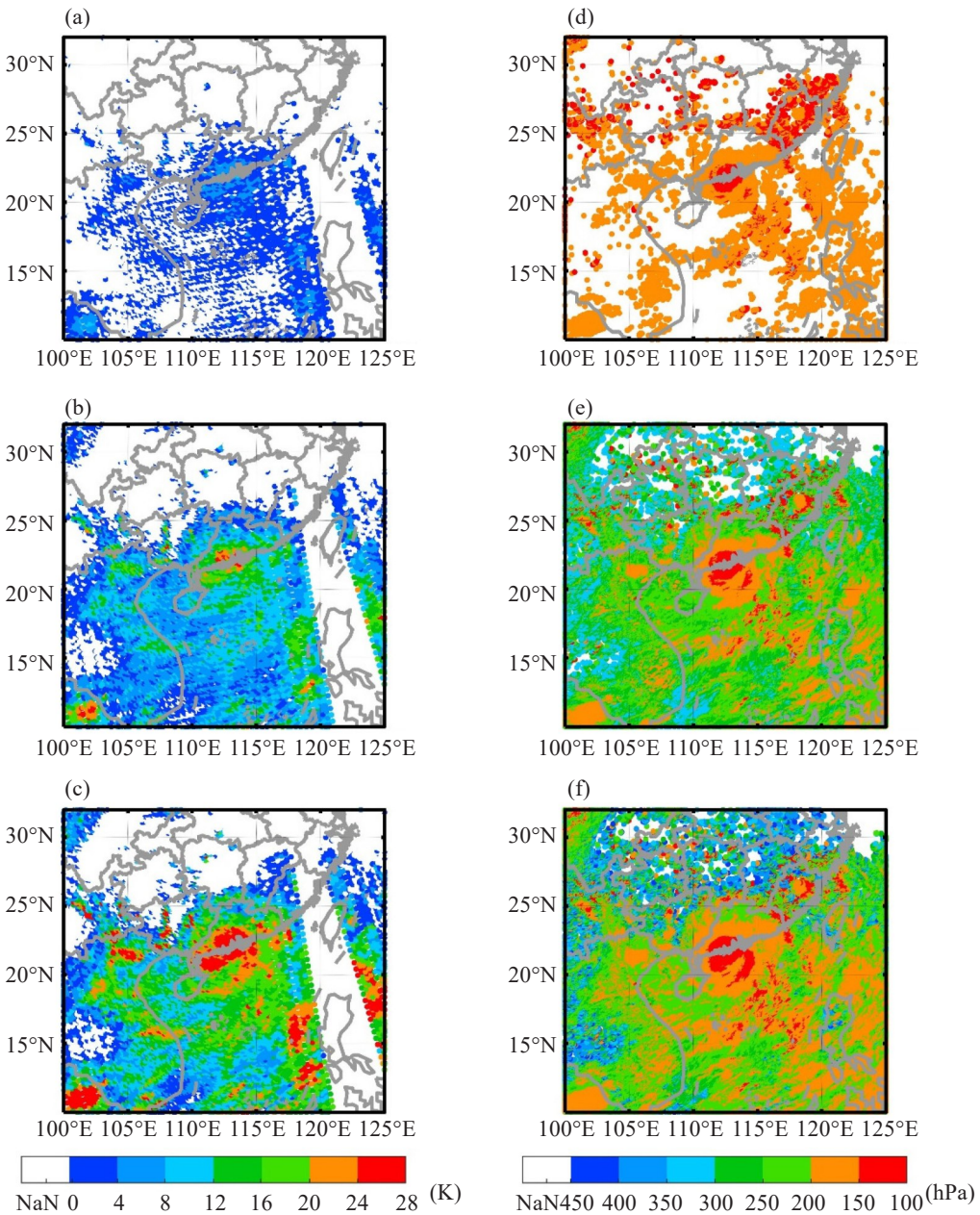

Figure 8. The same as Fig. 6 but for the ascending nodes at 05:46 UTC on 23 August 2017.

4.3 *Ice cloud detection performance compared with L17*

In L17, the performance of CESI with peak WF ~ 321 hPa is good compared with the distribution of ice cloud optical depth from AIRS. In this study, we used observational data to replace simulation from ECMWF 83 profiles and used stricter cloud insensitive condition to derive CESI. Fig. 11 shows the spatial distribution of Pair-3 (WFP~321 hPa) CESI derived from Lin and Pair-3 (WFP~320 hPa) from our work in the ascending nodes on August 23, 2017, respectively. It shows that the patterns of CESI agree with each other for detecting ice clouds located around 320 hPa but the values of CESI from this work is larger than it from L17. One of the reasons is that it lacks the geometry information of satellite and solar that would affect the measurements of *BT* from SWIR channels in the process of L17 during the daytime. Compared with cloud types from Himawari-8 (Fig. 9), the red circle areas in Fig. 11 are categorized as cirrostratus that are not detected by CESI derived from L17 but can be measured by CESI from this study. In other words, a better cloud detection can be derived from real observations.

Although the CESI can detect ice clouds in different layers, there are still some limitations. First, the

SWIR channels may be affected by the noise, especially for the high WF altitude pairs of CESI, which would lead to larger bias of cloud detection. In Fig. 6a and 8a, Pair-1 with WF peak altitude around 160 hPa shows that the cloud features are not clear. Second, the cloud detection thresholds for each layers of CESI are not derived, which will be obtained by integrating the active sensor (such as CALIPSO or CloudSat) in the future.

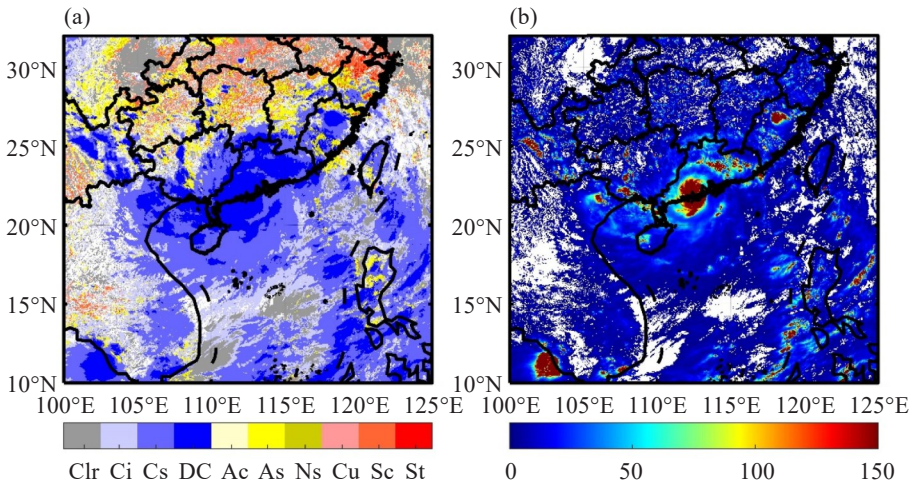

Figure 9. Spatial distribution of (a) cloud types from Himawari-8 at 05:50 on 23 August: clear (labeled Clr), cirrus (labeled Ci), cirrostratus (labeled Cs), deep convection (labeled DC), altocumulus (labeled Ac), altostratus (labeled As), nimbostratus (labeled Ns), cumulus (labeled Cu), stratocumulus (labeled Sc), and stratus (labeled St); (b) cloud optical thickness from Himawari-8 at 05:50 on 23 August.

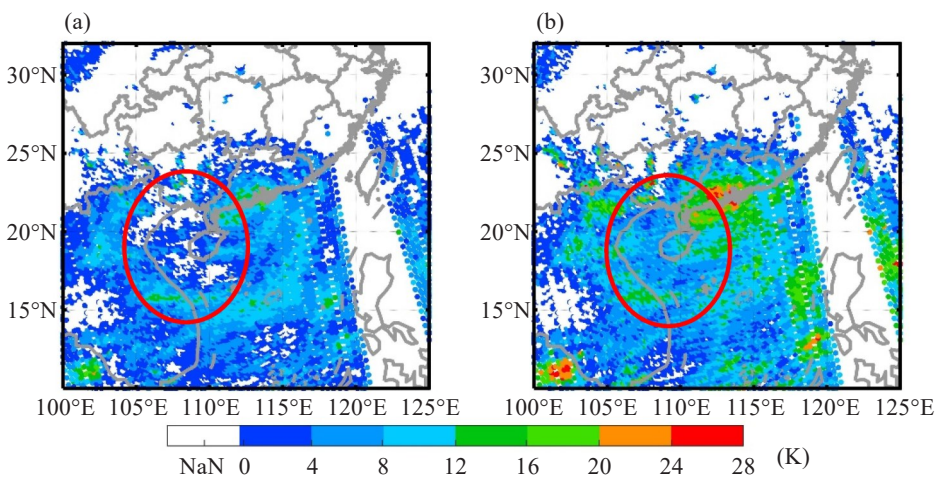

Figure 10. (a) Spatial distribution of CESI derived from L17 (peak WF~321hPa); (b) spatial distribution of CESI in this study (peak WF~320hPa).

5 CONCLUSION

Ice clouds cover around 20% of the globe. Detecting ice clouds in different layers using infrared sensors is still a challenge. Lin et al. developed a new algorithm to detect clouds in different levels by combining LWIR and SWIR CO_2 absorption bands from the Cross-Track Infrared Sounder (CrIS) [21]. The algorithm, i. e., Cloud Emission and Scattering Index (CESI), is based on the difference in scattering and emission characteristics between LWIR and SWIR channels. Based on Lin's method, the present study uses CO_2 LWIR and SWIR channels from CrIS SDR full spectrum resolution data to improve the vertical resolution of ice clouds. Additionally, there are two differences between our work and L17 in pairing longwave and shortwave of CO_2 channels. First, the training data sets are randomly chosen from eight days in four seasons to find the observational clear profiles according to VIIRS EDR cloud mask products. The "confident" clear and high-quality data are selected from VIIRS pixels that are fully occupied in FOV from CrIS. The day and night conditions are considered in this study as well, because of the diurnal variations. Second, the conditions of insensitive level for shortwave channels in the present study is stricter than those in L17, and they help the CESI values present cloud layers more obviously. Furthermore, the CrIS full spectrum

resolution data is used to improve the vertical resolution. The CESI captures the center and cloud features of super typhoon Hato located above 415 hPa.

The CESI can detect ice clouds in different layers; however, there are still some limitations. First, the SWIR channels, especially the high WF altitude pairs of CESI, may be affected by the noise. Second, the cloud detection thresholds for each layers of CESI are not derived, which will be obtained in the future.

REFERENCES

[1] SASSEN K, WANG Z, LIU D. Global distribution of cirrus clouds from CloudSat / Cloud-Aerosol Lidar and Infrared Pathfinder Satellite Observations (CALIPSO) measurements [J]. J Geophys Res: Atmos, 2008, 113: D00A12, https://doi.org/10.1029/2008JD009972.

[2] LIOU K N. Influence of cirrus clouds on weather and climate processes: A global perspective [J]. Mon Wea Rev, 1986, 114(6): 1167-1199, https://doi. org / 10.1175 / 1520-0493(1986)1142.0.CO;2.

[3] STEPHENS G L, TSAY S C, STACKHOUSE Jr P W, et al. The relevance of the microphysical and radiative properties of cirrus clouds to climate and climatic feedback [J]. J Atmos Sci, 1990, 47(14): 1742-1754, https://doi.org/10.1175/1520-0469(1990)047<1742:TROTMA>2.0.CO;2.

[4] INOUE T. On the temperature and effective emissivity determination of semi-transparent cirrus clouds by bi-spectral measurements in the 10μm window region [J]. J Meteor Soc Japan, 1985, 63(1): 88-99, https://doi. org / 10.2151/jmsj1965.63.1_88.

[5] ACKERMAN S A, SMITH W, REVERCOMB H, et al. The 27–28 October 1986 FIRE IFO cirrus case study: Spectral properties of cirrus clouds in the 8–12 μm window [J]. Mon Wea Rev, 1990, 118(11): 2377-2388, https://doi.org/10.1175/1520-0493(1990)118<2377:TOFICC>2.0.CO;2.

[6] PAROL F, BURIEZ J, BROGNIEZ G, et al. Information content of AVHRR channels 4 and 5 with respect to the effective radius of cirrus cloud particles [J]. J Appl Meteor, 1991, 30(7): 973-984, https://doi.org / 10.1175 / 1520-0450-30.7.973.

[7] GIRAUD V, BURIEZ J, FOUQUART Y, et al. Large-scale analysis of cirrus clouds from AVHRR data: Assessment of both a microphysical index and the cloud-top temperature [J]. J Appl Meteor, 1997, 36(6): 664-675, https://doi. org / 10.1175/1520-0450-36.6.664.

[8] CHIRIACO M, CHEPFER H, NOEL V, et al. Improving retrievals of cirrus cloud particle size coupling lidar and three-channel radiometric techniques [J]. Mon Wea Rev, 2004, 132(7): 1684-1700, https://doi. org / 10.1175 / 1520-0493(2004)132<1684:IROCCP>2.0.CO;2.

[9] PRABHAKARA C, FRASER R, DALU G, et al. Thin cirrus clouds: Seasonal distribution over oceans deduced from Nimbus-4 IRIS [J]. J Appl Meteor, 1988, 27(4): 379-399, https://doi. org / 10.1175 / 1520-0450(1988)027<0379:TCCSDO>2.0.CO;2.

[10] HEIDINGER A K, PAVOLONIS M J. Gazing at cirrus clouds for 25 years through a split window, Part I: Methodology [J]. J Appl Meteor Climatol, 2009, 48(6): 1100-1116, https://doi.org/10.1175/2008JAMC1882.1.

[11] WANG C, YANG P, BAUM B A, et al. Retrieval of ice cloud optical thickness and effective particle size using a fast infrared radiative transfer model [J]. J Appl Meteor Climatol, 2011, 50(11): 2283-2297, https://doi. org / 10.1175/JAMC-D-11-067.1.

[12] KOPP T J, THOMAS W, HEIDINGER A K, et al. The VIIRS Cloud Mask: Progress in the first year of S-NPP toward a common cloud detection scheme [J]. J Geophys Res: Atmos, 2014, 119(5): 2441-2456, https://doi. org / 10.1002/2013JD020458.

[13] OU S, LIOU K, YANG P, et al. Airborne retrieval of cirrus cloud optical and microphysical properties using Airborne Remote Earth Sensing System 5.1–5.3 and 3.7-μm channel data [J]. J Geophys Res: Atmos, 1998, 103 (D18): 23231-23242, https://doi.org/10.1029/98JD02069.

[14] MCNALLY A, WATTS P. A cloud detection algorithm for high - spectral - resolution infrared sounders [J]. Quart J Roy Meteor Soc, 2003, 129(595): 3411-3423, https://doi.org/10.1256/qj.02.208.

[15] MENZEL W P, SCHMIT T J, ZHANG P, et al. Satellite-based atmospheric infrared sounder development and applications [J]. Bull Amer Meteor Soc, 2018, 99(3): 583-603, https://doi.org/10.1175/BAMS-D-16-0293.1.

[16] CHAHINE M T. Remote sounding of cloudy atmospheres, I: The single cloud layer [J]. J Atmos Sci, 1974, 31(1): 233-243, https://doi. org / 10.1175 / 1520-0469(1974)031<0233:RSOCAI>2.0.CO;2.

[17] SMITH W, PLATT C. Comparison of satellite-deduced cloud heights with indications from radiosonde and ground-based laser measurements [J]. J Appl Meteor, 1978, 17(12): 1796-1802, https://doi. org / 10.1175 / 1520-0450(1978)017<1796:COSDCH>2.0.CO;2.

[18] MENZEL W, SMITH W, STEWART T. Improved cloud motion wind vector and altitude assignment using VAS [J]. J Clim Appl Meteor, 22: 377-384, https://doi. org / 10.1175 / 1520-0450(1983)022<0377: ICMWVA>2.0. CO; 2.

[19] SMITH W L, FREY R. On cloud altitude determinations from high resolution interferometer sounder (HIS) observations [J]. J Appl Meteor, 1990, 29(7): 658-662, https://doi. org / 10.1175 / 1520-0450(1990)029<0658:OCADFH>2.0.CO;2.

[20] GAO B, LI R, SHETTLE E. Cloud remote sensing using midwave IR CO_2 and N_2O slicing channels near 4.5 μm [J]. Remote Sens, 2011, 3(12): 1006-1013, https://doi.org/10.3390/rs3051006.

[21] LIN L, ZOU X, WENG F. Combining CrIS double CO_2 bands for detecting clouds located in different layers of the atmosphere [J]. J Geophys Res: Atmos, 2017, 122(3): 1811-1827, https://doi.org/10.1002/2016JD025505.

[22] HAN Y, REVERCOMB H, CROMP M, et al. Suomi NPP CrIS measurements, sensor data record algorithm, calibration and validation activities, and record data quality [J]. J Geophys Res: Atmos, 2013, 118(22): 12734-12748, https://doi.org/10.1002/2013JD020344.

[23] CHEN Y, HAN Y, TREMBLAY D, et al. CrIS Full Resolution Processing and Validation System for JPSS [C]// 19th International TOVS Study Conference (ITSC), Jeju Island: The International TOVS Working Group, 2014: 1-12.

[24] CHEN Y, HAN Y, WENG F. Characterization of long-term stability of Suomi NPP Cross-track Infrared Sounder spectral calibration [J]. IEEE Trans Geosci Remote Sens,

2017, 55(2): 1147-1159, https://doi. org / 10.1109 / TGRS.2016.2620438.

[25] HAN Y, CHEN Y. Calibration algorithm for Cross-track Infrared Sounder full spectral resolution measurements [J]. IEEE Trans Geosci Remote Sens, 2018, 56(2): 1008-1016, https://doi.org/10.1109/TGRS.2017.2757940.

[26] CAO C, XIONG J, BLONSKI S, et al. Suomi NPP VIIRS sensor data record verification, validation, and long-term performance monitoring [J]. J Geophys Res: Atmos, 2013, 118(20): 11664-11678, https://doi. org / 10.1002 / 2013JD020418.

[27] HUTCHISON K D, ROSKOVENSKY J K, JACKSON J M, et al. Automated cloud detection and classification of data collected by the Visible Infrared Imager Radiometer Suite (VIIRS) [J]. Int J Remote Sens, 2005, 26(2): 4681-4706, https://doi.org/10.1080/01431160500196786.

[28] WENG F, HAN Y, van DELST P, et al. JCSDA Community Radiative Transfer Model (CRTM) [C]// 14th International TOVS Study Conference. Beijing: The International TOVS Working Group, 2005: 217-222.

[29] CHEN Y, HAN Y, van DELST, et al. Assessment of shortwave infrared sea surface reflection and nonlocal thermodynamic equilibrium effects in the community radiative transfer model using IASI data [J]. J Atmos Oceanic Technol, 2013, 30(9): 2152-2160, https://doi.org/10.1175/JTECH-D-12-00267.1.

[30] YANG P, WEI H, HUANG H, et al. Scattering and absorption property database for nonspherical ice particles in the near-through far-infrared spectral region [J]. Appl Opt, 2005, 44(26): 5512-5523, https://doi. org / 10.1364/AO.44.005512.

[31] van DELST P, WU X. A high resolution infrared sea surface emissivity database for satellite applications [C]// 11th International TOVS Study Conference, Budapest: The International TOVS Working Group, 2000: 407-411.

[32] WU X, SMITH W L. Emissivity of rough sea surface for 8–13 μm: modeling and verification [J]. Appl Opt, 1997, 36(12): 2609-2619, https://doi. org / 10.1364 / AO.36.002609.

[33] LIU Q, BOUKABARA S. Community Radiative Transfer Model (CRTM) applications in supporting the Suomi National Polar-orbiting Partnership (SNPP) mission validation and verification [J]. Remote Sens Environ, 2014, 140: 744-754, https://doi. org / 10.1016 / j. rse.2013.10.011.

[34] WANG L, TREMBLAY D, ZHANG B, et al. Fast and accurate collocation of the visible infrared imaging radiometer suite measurements with cross-track infrared sounder [J]. Remote Sens, 2016, 8(1): 76, https://doi.org/10.3390/rs8010076.

[35] ROSSOW W B, SCHIFFER R A. Advances in understanding clouds from ISCCP [J]. Bull Amer Meteor Soc, 1999, 80(11): 2261-2288, https://doi. org / 10.1175 / 1520-0477(1999)080%3C2261:AIUCFI%3E2.0.CO;2.

[36] WENG F, ZOU X. 30-Year atmospheric temperature record derived by one-dimensional variational data assimilation of MSU / AMSU-A observations [J]. Clim Dyn, 2014, 43(7): 1857-1870, https://doi. org / 10.1007 / s00382-013-2012-5.

[37] CARRIER M, ZOU X, LAPENTA W M. Identifying cloud-uncontaminated AIRS spectra from cloudy FOV based on cloud-top pressure and weighting functions [J]. Mon Wea Rev, 2007, 135(6): 2278-2294, https://doi. org / 10.1175/MWR3384.1.

[38] HAN Y, ZOU X, WENG F. Cloud and precipitation features of Super Typhoon Neoguri revealed from dual oxygen absorption band sounding instruments on board Fengyun-3C satellite [J]. Geophys Res Lett, 2015, 42(3): 916-924, https://doi.org/10.1002/2014GL062753.

[39] WANG L, TIAN M, ZHENG Y. Assessment and improvement of the Cloud Emission and Scattering Index (CESI) - an algorithm for cirrus detection [J]. Int J Remote Sens, 2019, 40(14): 5366-5387, https://doi. org / 10.1080/01431161.2019.1579938.

[40] WANG L, ZHENG Y, LIU C, et al. Combination of AIRS dual CO_2 absorption bands to develop an ice clouds detection algorithm in different atmospheric layers [J]. Remote Sens, 2020, 12(1): 6, https://doi. org / 10.3390 / rs12010006.

[41] NIU Z, ZOU X. A potential application of height-dependent cloud emission and scattering indices for identifying CrIS clear channels above clouds [J]. Tellus A, 2020, 72(1): 1-21, https://doi. org / 10.1080 / 16000870.2019.1696141.

[42] KAHN B H, LIOU K N, LEE S Y, et al. Nighttime cirrus detection using atmospheric infrared sounder window channels and total column water vapor [J]. J Geophys Res: Atmos, 2015, 110: D07203, https://doi.org/10.1029/2004JD005430.

Citation: WANG Li-wen, ZHENG You-fei, TIAN Miao, et al. An algorithm for detecting ice cloud at different altitudes by combining dual CrIS full spectrum resolution CO_2 channels [J]. J Trop Meteor, 2020, 26(3): 300-310, https: //doi. org / 10.46267 / j. 1006-8775.2020.027.